

Experimental validation of state equations and dynamic route maps for phase change memristive devices

Original

Experimental validation of state equations and dynamic route maps for phase change memristive devices / Marrone, Francesco; Secco, Jacopo; Kersting, Benedikt; Le Gallo, Manuel; Corinto, Fernando; Sebastian, Abu; Chua, Leon O. - In: SCIENTIFIC REPORTS. - ISSN 2045-2322. - 12:1(2022), pp. 1-10. [10.1038/s41598-022-09948-6]

Availability:

This version is available at: 11583/2996378 since: 2025-01-08T13:47:34Z

Publisher:

Nature Research

Published

DOI:10.1038/s41598-022-09948-6

Terms of use:

This article is made available under terms and conditions as specified in the corresponding bibliographic description in the repository

Publisher copyright

(Article begins on next page)



OPEN

Experimental validation of state equations and dynamic route maps for phase change memristive devices

Francesco Marrone¹✉, Jacopo Secco¹, Benedikt Kersting², Manuel Le Gallo², Fernando Corinto¹✉, Abu Sebastian²✉ & Leon O. Chua³

Phase Change Memory (PCM) is an emerging technology exploiting the rapid and reversible phase transition of certain chalcogenides to realize nanoscale memory elements. PCM devices are being explored as non-volatile storage-class memory and as computing elements for in-memory and neuromorphic computing. It is well-known that PCM exhibits several characteristics of a memristive device. In this work, based on the essential physical attributes of PCM devices, we exploit the concept of *Dynamic Route Map* (DRM) to capture the complex physics underlying these devices to describe them as memristive devices defined by a state-dependent Ohm's law. The efficacy of the DRM has been proven by comparing numerical results with experimental data obtained on PCM devices.

PCM devices encode information on the phase configuration of a layer of material sandwiched between two metallic electrodes. This class of materials, typically compounds of Ge, Te and Sb exhibit a high electric conductivity in the crystalline phase and a much lower conductivity in the amorphous phase. In recent years, PCM devices have found application in stand-alone storage class memory¹, embedded memory for edge computing², reconfigurable electronics³ as well as neuromorphic^{4,5} and in-memory computing^{6–8}.

A prototypical mushroom-type PCM⁹ device is schematically shown in Fig. 1a. A PCM device consists of a certain volume of phase change material sandwiched between the top and bottom metal electrodes. Applying current pulses to the device results in significant heating due to Joule heating. A RESET pulse refers to a current pulse which can melt a significant portion of the phase change material. When the pulse is stopped abruptly, the molten material quenches into the amorphous phase due to glass transition. In the resulting RESET state, the device will be in a high resistance state provided, the amorphous region blocks the bottom electrode. When a current pulse (typically referred to as the SET pulse) is applied to a PCM device in the RESET state, a part of the amorphous region crystallizes. Thus by modulating the size of the amorphous region by the application of suitable SET pulses, it is possible to achieve a continuum of resistance or conductance states. The resistance state achieved after the application of RESET or SET pulses can be deciphered by biasing the device with a small amplitude read voltage that does not disturb the phase-configuration.

PCM devices exhibit intriguing nonlinear dynamical behavior arising from a complex interaction among thermal, electrical and structural dynamics¹⁰. Accurate physical models exploiting integro-differential equations have been derived to capture the peculiar characteristic of the different operating conditions in PCM devices and then numerical analysis is essential to accurately describe the experimental observations¹¹. However, it will be very interesting to describe the PCM device dynamics described as a memristive system as introduced in 1976 by S. Kang and L. O. Chua¹². The pinched *current-voltage* loop characteristics shown by PCM devices under bipolar periodic input, as exemplified in Fig. 1b, clearly casts them in the class of memristive systems. In this work, our objective is to represent PCM devices via a state-dependent Ohm's law, that is the Ohm's law $v = R(\mathbf{x}, i)i$ linking voltage v across and current i through the two-terminal memristive device and a state equation $\dot{\mathbf{x}} = f(\mathbf{x}, i)$ governing the dynamics of the internal state variables, \mathbf{x} . The use of the memristive state-dependent Ohm's law facilitates the visualization of the complex dynamics in PCM cells in terms of concepts such as Dynamic Route Maps (DRM) and the Power-Off-Plots (POP)¹³. When the state variable is scalar ($x \in \mathbf{R}$), the DRM represents

¹Department of Electronics and Telecommunications, Politecnico di Torino, Torino 10129, Italy. ²IBM Research - Zurich, Rüschlikon 8803, Switzerland. ³Department of Electrical Engineering and Computer Sciences, University of California, Berkeley 94720, CA, USA. ✉email: francesco.marrone@polito.it; fernando.corinto@polito.it; ase@zurich.ibm.com

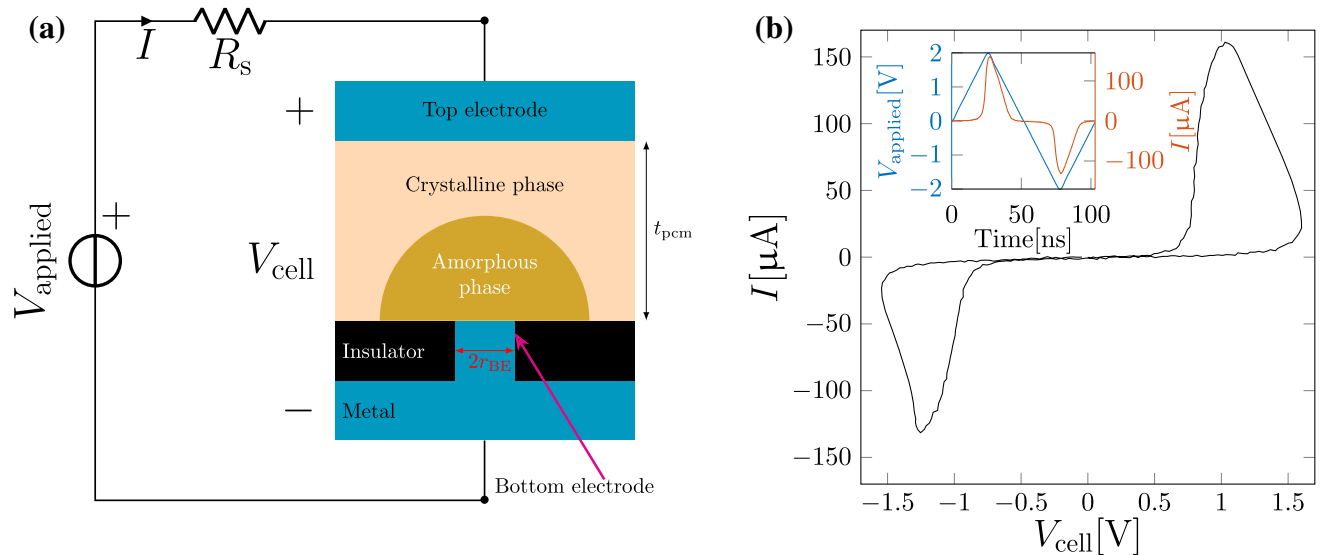


Figure 1. Mushroom-type PCM device and memristive characteristics. **(a)** Schematic representation of a mushroom-type PCM device operated with an integrated current compliance series resistor R_s . When the amorphous phase blocks the bottom electrode, the device is in a high-resistance state. The effective thickness of the amorphous region is denoted by u_a . V_{applied} is the externally applied input voltage, I is the current flowing through the PCM device and $V_{\text{cell}} = V_{\text{applied}} - R_s I$ is the intrinsic voltage drop on the device. **(b)** The measured current-voltage relationship on the mushroom-type PCM device highlighting the pinched hysteresis loop characteristic of memristive devices.

the plot of $f(x, i)$ in the plane (\dot{x}, x) ; each DRM is parametrized by the input i and then a family of curves that span the whole plane (\dot{x}, x) . If $i = 0$ then the DRM results into the POP and describe the long-term behavior of the memristive devices and their memory properties. Such a circuit-theoretic model is capable of accurately describing the electrical measurements and capturing the device physics in some key parameters. The use of DRMs, in addition, has been found to be a useful modeling method in recent years for similar devices. Ascoli *et al.* showed that such techniques can be exploited to investigate theoretically all the scenarios of the switching dynamics in memristive devices¹⁴. Subsequently, other works have shown how DRMs can be a powerful tool to model other devices such as ReRAMs, or of complex systems such as *Cellular Nonlinear Networks*^{15,16}. In this work, we provide for the first time an experimental validation of these techniques for phase-change memory devices.

Results

Memristive state equations. First, we will derive the memristive state equations based on the PCM device characteristics. A useful schematic illustration of the convoluted interconnections between the electrical, thermal and structural dynamics in PCM devices is reported in Fig. 2. The thickness of the amorphous region, u_a , is one of the key state variables. Another key variable is the temperature at the interface of the amorphous and crystalline regions denoted by T_{int} .

When an electrical pulse is applied to a PCM device, the voltage dropped across the device is denoted by V_{cell} . Depending on V_{cell} , the device could be in a low-field *OFF-state* or a high-field *ON-state*. In the *OFF-state*, the device conductance exhibits for increasing applied electric fields, linear, exponential and super-exponential dependence on V_{cell} ¹⁷. In the *ON-state*, conduction through the amorphous phase is metal-like and the global flow of electrons in the PCM cell becomes dominated by the amorphous-crystalline Schottky barrier¹⁸. The rather complex transition between the OFF and ON states happens via the so called threshold switching event, the physical mechanism for which is being actively researched¹¹. It is observed that threshold switching occurs once the current flowing through the device exceeds a fixed current, I_{TH} ¹¹ typically in the range of 10 μA .

A “write pulse” typically refers to an electrical pulse that results in a change in the phase-configuration. During the application of the write pulse, the device has to go to the *ON-state* since only in the *ON-state* is there sufficient power dissipation and structural dynamics to induce any meaningful change in u_a . If the write pulse amplitude is sufficiently large that the $T_{\text{int}}(u_a)$ exceeds the melting temperature, T_{melt} , then u_a increase in such a way that $T_{\text{int}}(u_a) = T_{\text{melt}}$. And if at this point, the pulse amplitude is abruptly brought to zero, then there is not enough time for crystallization and via the melt-quench process, a new amorphous region is created with the corresponding u_a . These type of pulses are referred to as RESET pulses and the amplitude of the write pulses are denoted by I_{RESET} .

In this work, we study write pulses that have sufficiently small amplitude (referred to as SET pulses) such that u_a reduces due to crystal growth. We first initialize the device with an appropriate RESET pulse to achieve an initial u_a . When such a write pulse is applied, the current flowing through the cell is denoted by I and the dissipated power is $P = V_{\text{cell}} I$. This results in an increase in T_{int} which in turn will trigger a significant change in the rate of crystal growth. This alters the size of the amorphous region and in particular, u_a . In the *ON-state*, the

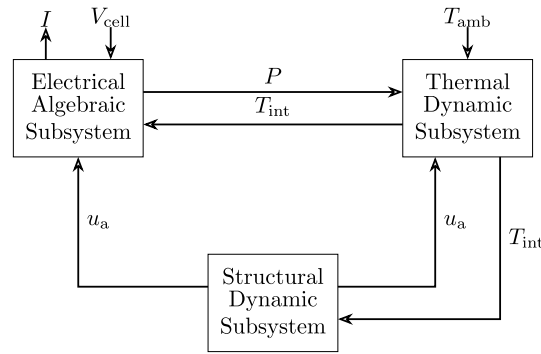


Figure 2. PCM dynamics. Block diagram illustration of the interplay between the electrical, thermal and structural dynamics in a PCM device. The system has two inputs V_{cell} and T_{amb} and one output I . V_{cell} is the voltage drop on the PCM device. T_{amb} denotes the ambient temperature at which the device is operated. I is the current flowing through the device. P is the electrical power dissipated by the device and is computed as the product between I and V_{cell} . u_a is the effective thickness of the amorphous region and its evolution is determined by the crystallization dynamics. T_{int} is the temperature at the amorphous-crystalline interface and its evolution is determined by the heat balance equation.

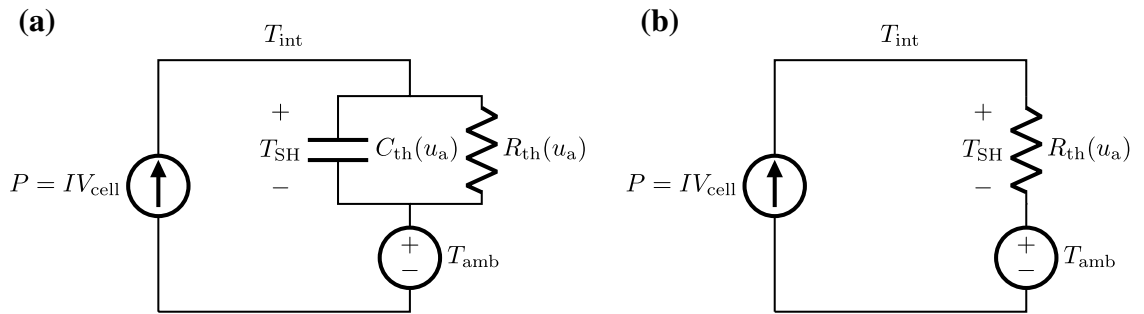


Figure 3. Thermal subsystem. (a) First order circuit model that takes into account the presence of $C_{th}(u_a)$ (see Eq. (1)). (b) The simplified circuit model can be employed as described by Eq. (2) when the write pulse duration is substantially higher than τ_{th} .

resistance of the device is not indicative of u_a as described earlier. Hence to decipher the phase-configurational information, the only way is to operate the device at the low-field *OFF-state*. This is typically referred to as the read operation. A more detailed analysis of the three key dynamical subsystems is presented next.

Thermal subsystem. The thermal subsystem captures the evolution of the interface temperature, T_{int} upon the dissipation of power, P , in the device upon the application of an electrical pulse (see Fig. 3). $T_{int} = T_{amb} + T_{sh}$ where T_{amb} is the ambient temperature and T_{sh} is the cell Joule self-heating temperature increment. T_{sh} evolves according to,

$$\frac{d}{dt} T_{sh}(t) = \frac{1}{\tau_{th}} (R_{th}(u_a(t))P - T_{sh}(t)) \tag{1}$$

where $\tau_{th} = R_{th}(u_a(t))C_{th}(u_a(t))$ is the thermal time constant and $R_{th}(u_a(t))$, shown in Fig. 4a, is the amorphous-thickness-dependent thermal resistance of the device which was estimated via finite element modelling (FEM)¹⁹. The thermal time constant was found to be on the order of a nanosecond¹⁰. Hence, for write pulses of duration larger than 10 ns, (1) can be reduced to an algebraic equation as

$$T_{sh} = R_{th}(u_a)P \tag{2}$$

and

$$T_{int} = T_{amb} + R_{th}(u_a)P \tag{3}$$

Moreover, a good linear approximation of R_{th} can be given, in the blocked bottom electrode condition, as

$$R_{th}(u_a(t)) = -\kappa u_a(t) + R_{th,0} \tag{4}$$

where, $\kappa \approx -0.024 \frac{K}{\mu W nm}$ and $R_{th,0} \approx 1.908 \frac{K}{\mu W}$. Hence the interface temperature is assumed to instantly vary with the dissipated power as shown by the circuit representation in Fig. 3b.

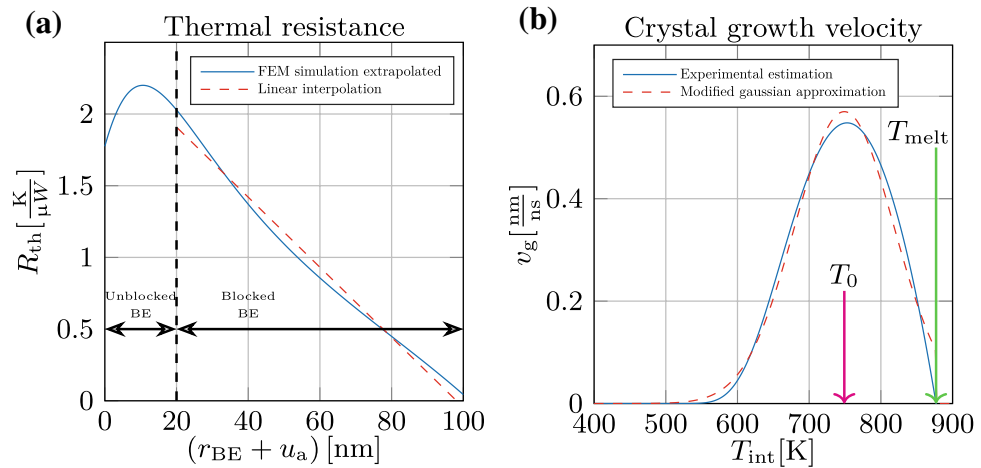


Figure 4. Effective thermal resistance and crystal growth velocity. **(a)** The effective thermal resistance of a mushroom-type PCM device as a function of the amorphous thickness u_a . This is obtained from Finite-element modeling that was also experimentally corroborated by Sebastian et al.¹⁹. Also shown is a linear approximation of the effective thermal resistance in the scenario where the bottom-electrode is fully blocked by the amorphous region (dashed-red line). **(b)** The experimentally measured crystal growth velocity $v_g(T_{int})$ as a function of the interface temperature T_{int} based on Sebastian et al.¹⁹. Also shown is a Gaussian approximation (dashed-red line).

Structural dynamic subsystem. The structural dynamic subsystem describes the evolution of the state variable, u_a . The evolution of u_a is dictated by the temperature-driven crystallization dynamics given by,

$$\frac{d}{dt} u_a(t) = -v_g(T_{int}(t)) \tag{5}$$

where $u_a \in [0,80] \text{ nm}$.

The crystal growth velocity, v_g , has a strong temperature dependence and was experimentally measured by Sebastian et al.¹⁹. A Gaussian approximation of $v_g(T_{int})$, shown in Fig. 4b, has also already been proposed by Secco et al.²⁰, given by,

$$v_g(T_{int}) = A_{v_g} \exp \left[- \left(\frac{T_{int} - T_0}{\sigma_T} \right)^2 \right] \tag{6}$$

$A_{v_g} \approx 0.57 \text{ nm}/\text{ns}$, $T_0 \approx 749 \text{ K}$ and $\sigma_T \approx 98 \text{ K}$. Note that, the changes of the material characteristics of the amorphous phase such as structural relaxation²¹ are not taken into account in this model. In the experimental data studied later, this effect was considered negligible due to the narrow time window over which the measurements are made.

Electrical subsystem. Next we consider the electrical subsystem which capture the electrical transport in a PCM device. The electrical transport is dominated by the more resistive amorphous region. As indicated earlier, there are two distinct regions of interest when it comes to the electrical subsystem. Here, we will delve a bit deeper into the *OFF-state* electrical transport that is relevant for the read operation. During read operation, there is minimal self heating and hence the temperature of the amorphous region can be assumed to be uniformly equal to T_{amb} .

More and more refined models have been developed over the years to explain how the two state variables (u_a, T_{amb}) influence the electron conduction through the material in the *OFF-state*²²⁻²⁵. The 3D Poole-Frenkel²⁶⁻²⁸ emission of carriers from a two-center Coulomb potential was shown to best model in an unified manner the conduction in the amorphous phase-change material for a wide range of fields, F . According to this model, the density of free carriers under an applied field $F = V_{cell}/u_a$ at T_{amb} is

$$n(F, T_{amb}) = \frac{K}{2} \int_0^\pi \exp \left(- \frac{E_a(T_{amb}) - E_{PF}(F, \theta)}{k_B T_{amb}} \right) \sin(\theta) d\theta$$

where $E_a(T_{amb})$ is the interface temperature dependent activation energy

$$E_a(T_{amb}) = E_{a,0} - \frac{a T_{amb}^2}{b + T_{amb}}$$

and $E_{PF}(F, \theta)$ is the the energy barrier lowering between two adjacent potential wells due to the Poole-Frenkel effect and is computed as

Parameter	Value	Unit
$K\mu_0$	10^{22}	$\text{m}^{-1}\text{V}^{-1}\text{s}^{-1}$
$E_{a,0}$	225	meV
a	600	μeVK^{-1}
b	800	K
s	2.4	nm
v_{sat}/μ_0	50	$\text{V}\mu\text{m}^{-1}$
ϵ_r	10	

Table 1. Parameters associated with the electrical subsystem.

$$E_{\text{PF}}(F, \theta) = -\max_r \Phi(r, \theta, F)$$

where $\Phi(r, \theta, F) = -qFr \cos(\theta) - \frac{\beta^2}{4q}(\frac{1}{r} + \frac{1}{s-r}) + \frac{\beta^2}{qs}$ is the electrical potential profile, s is the distance between two defect centers and $\beta = \frac{q^2}{\sqrt{4\pi\epsilon_r\epsilon_0}}$.

Conductivity of the amorphous phase per unit of area can then be computed as

$$\sigma(F, T_{\text{amb}}) = q\mu(F)n(F, T_{\text{amb}})$$

where $\mu(F)$ is the field dependent carrier mobility given by $\mu(F) = \frac{\mu_0}{\sqrt{1+(\mu_0F/v_{\text{sat}})^2}}$. The current density $j(F, T_{\text{amb}})$ can be computed as $j(F, T_{\text{amb}}) = \sigma(F, T_{\text{amb}})F$. and the current flowing through the cell can be found by simply multiplying the current density $j(F, T_{\text{amb}})$ times the effective bottom electrode contact area A which is calculated through the effective bottom electrode radius and not the physical radius of the heater, $I(F, T_{\text{amb}}) = Aj(F, T_{\text{amb}})$. The model parameters are reported in Table 1.

State dependent Ohm’s law. To summarize, during the application of write pulses, when the device is biased at high field, it goes into a very low resistance state independent of the state variable u_a . As shown in Fig. 5a, the voltage drop V_{cell} is confined to a narrow voltage band around $V_{\text{cell,ON}} \approx 0.8$ V. This enables the simplification of the complex conduction mechanism to a simple nonlinear current-controlled resistor whose behavior for high enough currents can be well approximated by an ideal voltage generator of value $V_{\text{cell,ON}}$.

However, during read operation, we retrieve the phase-configurational information by application of a low amplitude current pulse. Under the hypothesis of fully blocked bottom electrode ($u_a > 0$) and very low-field ($F = \frac{V_{\text{cell}}}{u_a} \rightarrow 0$), the voltage can be well approximated by a linear relation $V_{\text{cell}} = R_m(u_a, T_{\text{amb}})I$, as shown in Fig. 5b, where the memristance $R_m(u_a, T_{\text{amb}})$ is given by

$$R_m(u_a, T_{\text{amb}}) = K' u_a \exp\left(\frac{E_a(T_{\text{amb}})}{k_B T_{\text{amb}}}\right) \tag{7}$$

being k_B the Boltzmann constant, $E_a(T_{\text{amb}})$, the temperature-dependent activation energy and $K' = \frac{1}{\pi^2 q_e K \mu_0}$. This expression for the memristance $R_m(u_a, T_{\text{amb}})$ can readily be derived from the Taylor series expansion of the Poole conduction model.

These aspects are summarized in the following state-dependent Ohm’s Law,

$$V_{\text{cell}} \approx \begin{cases} R_m(u_a, T_{\text{amb}})I & I \ll I_{\text{TH}} \\ 0.8V & I \gg I_{\text{TH}} \end{cases} \tag{8}$$

where the well-above-threshold-switching model ($I \gg I_{\text{TH}}$), depicted with circuitual symbolism in Fig. 5c, is intended to capture the cell power dissipation during the write phase. The interface temperature, T_{int} , is in turn a function of the dissipated power and the instantaneous u_a (see Equation (3)). The T_{int} in turn determines the crystal growth velocity which drives the structural dynamics and the evolution of u_a (see Equation (5)). Armed with these equations, we can explore the dynamic route maps of PCM devices. Finally, the well-below-threshold-switching model ($I \ll I_{\text{TH}}$), portrayed with circuitual symbolism in Fig. 5d gives a good approximation for the read phase where it is possible to observe the u_a state variable.

Dynamic route maps. Based on the state equations described in earlier sections, we performed a set of simulations to obtain the DRMs for the PCM device (see Fig. 6). The SET write pulse amplitude was varied from $I = 200 \mu\text{A}$ to $500 \mu\text{A}$. It can be seen that there is a significant dependence on the current amplitude. For example, for SET current amplitudes equal to or larger than $333 \mu\text{A}$, each route, when traversed, leads to a distinct nonzero equilibrium point. Whereas, for currents lower than $333 \mu\text{A}$, u_a becomes zero. The reason is that, for the larger RESET currents, as u_a reduces, T_{int} increases and eventually, it becomes equal to T_{melt} at which point crystal growth rate becomes zero. However, for lower RESET currents, T_{int} remains lower than T_{melt} resulting in a complete erasure of the amorphous region.

A key goal of this work is to experimentally measure the DRMs. To that end, we performed a set of experiments that involve applying SET pulses to the PCM device with a certain programming current but with varying

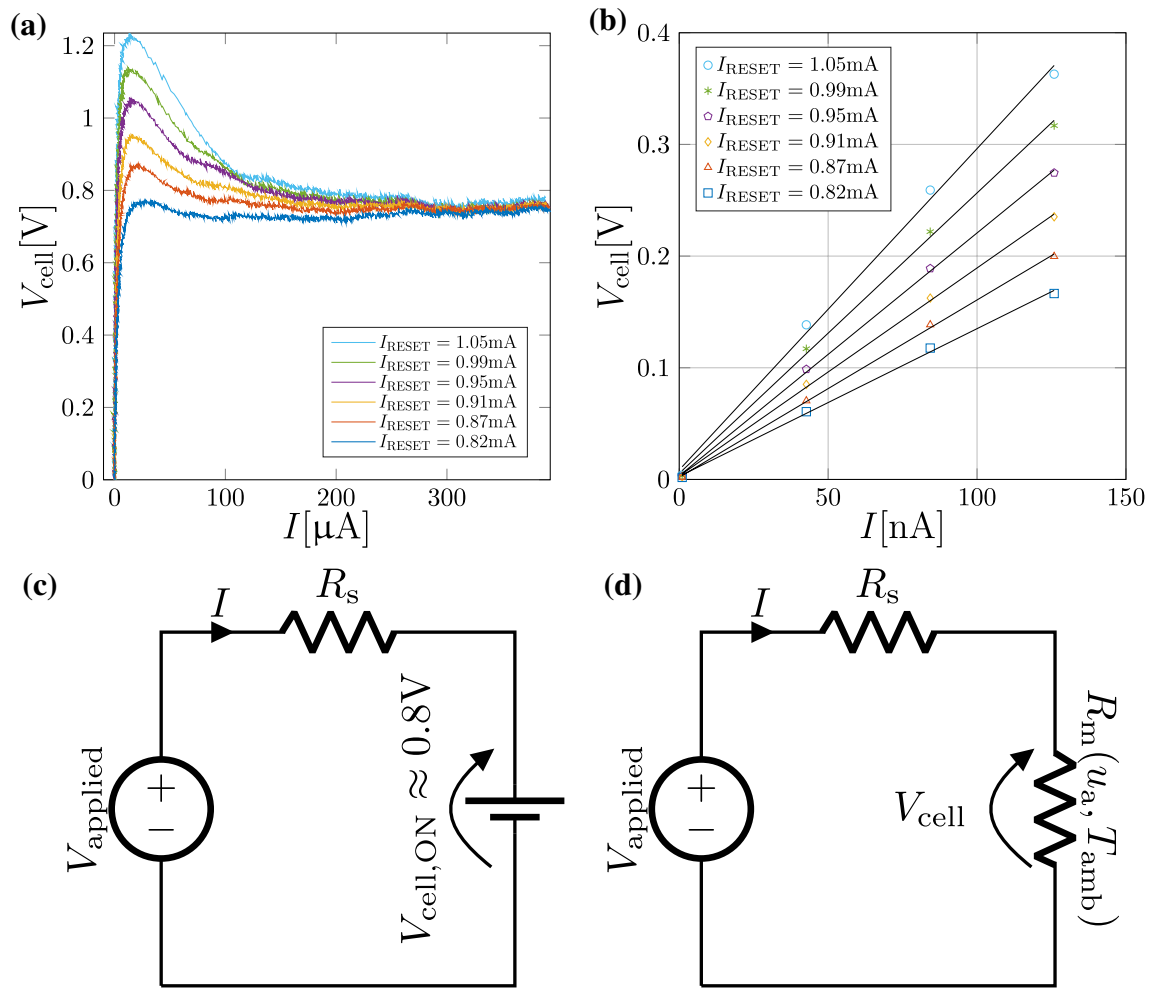


Figure 5. Electrical subsystem. (a) The measured $I - V_{\text{cell}}$ characteristics of the device when write pulses of different reset currents I_{RESET} are applied. It can be seen that beyond $I = 100 \mu\text{A}$, V_{cell} plateaus to approx. 0.8 V. (b) The low-field $I - V_{\text{cell}}$ characteristics are measured after the application of each write pulse. An almost linear behavior is observed. Moreover, the resistance progressively increases with increasing I_{RESET} . (c) During the application of the write pulse, the PCM device can be modeled as an ideal voltage generator $V_{\text{cell,ON}}$. (d) During read when probing the phase-configuration of the device, the PCM device can be modeled as a state-dependent linear resistor.

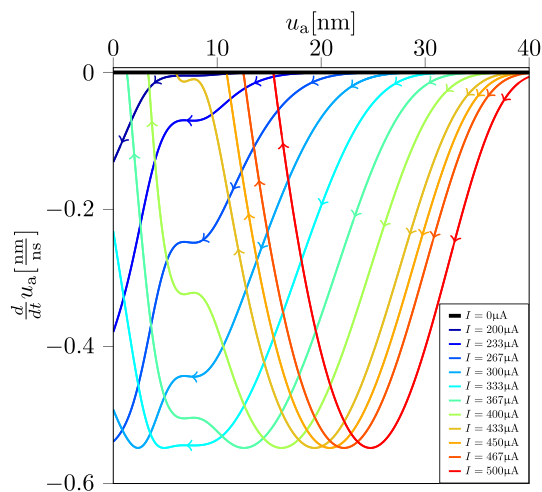


Figure 6. Dynamic route map for PCM. The computed dynamic route map for the PCM device corresponding to write pulses of varying amplitudes.

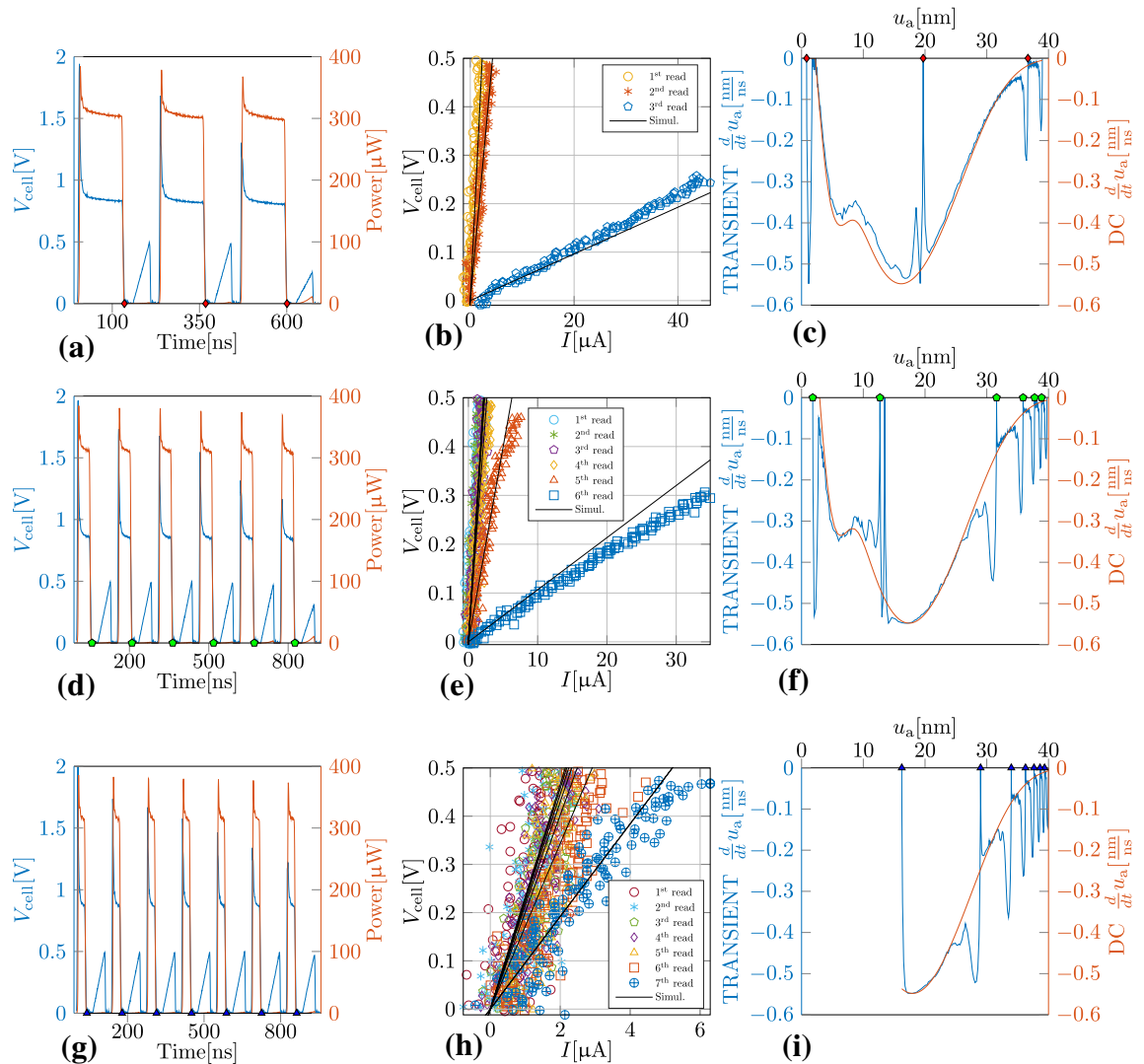


Figure 7. Experimental validation of DRM. Panels (a–c), (d–f) and (g–i) correspond to three separate experiments to measure the DRM. (Left column) Experimentally measured V_{cell} and the corresponding dissipated electrical power, P . Each square-shaped high-current write pulse is interleaved with a below threshold triangular read pulse (see Methods for more details). Between experiments, the key difference is the number and duration of the write pulses. (Center column) The $I - V_{\text{cell}}$ characteristics corresponding to the read pulses are shown. The effective amorphous thickness, u_a , is assumed to be directly proportional to the slope of these curves as per Eq. (7). (Right column) Based on the power signals shown on the left column, the u_a estimates based on the $I - V_{\text{cell}}$ characteristics shown in the center column and the memristive state equations, experimental DRMs are obtained (blue traces). Also shown are the DRMs based on the steady-state values of the power signals (red traces).

pulse duration (see Fig. 7). In the first experiment, we applied 3 pulses each of duration 121 ns (see Fig. 7a). After each pulse, we apply a triangular pulse with low amplitude to probe the low-field resistance and subsequently, to estimate u_a . We repeated this experiment two more times with more number of pulses with smaller duration. The smaller duration pulses facilitate more frequent probing of u_a during its evolution. Based on the experimental voltage and current traces, the dissipated power was calculated which in turn was used to calculate $\frac{du_a}{dt}$. In this manner, we could experimentally measure the DRM for the PCM device. As expected, all three experiments yielded comparable DRMs since the pulse amplitude was kept constant.

The DRMs can be used as a tool to tune the SET programming current to achieve a certain desired SET state. This is clear when looking at Fig. 6, starting from an high resistance RESET state associated with $u_a(t_0) \approx 50$ nm, the designer can choose to reach three different low resistance states by tuning the SET programming current. This in turn can be exploited to design programmable circuits such as programmable amplifiers and tunable filters. In the latter case, the knowledge about how the equilibria of u_a depend on the programming set current I_{SET} allows to precisely tune the position of zeros and poles in a completely analog fashion.

Let us consider a simple example where a PCM device is embedded into a passive (resistor-inductor-capacitor) RLC passband filter as reported in Fig. 8. Let us assume the input to be a small signal current $i_s(t)$ (e.g. current

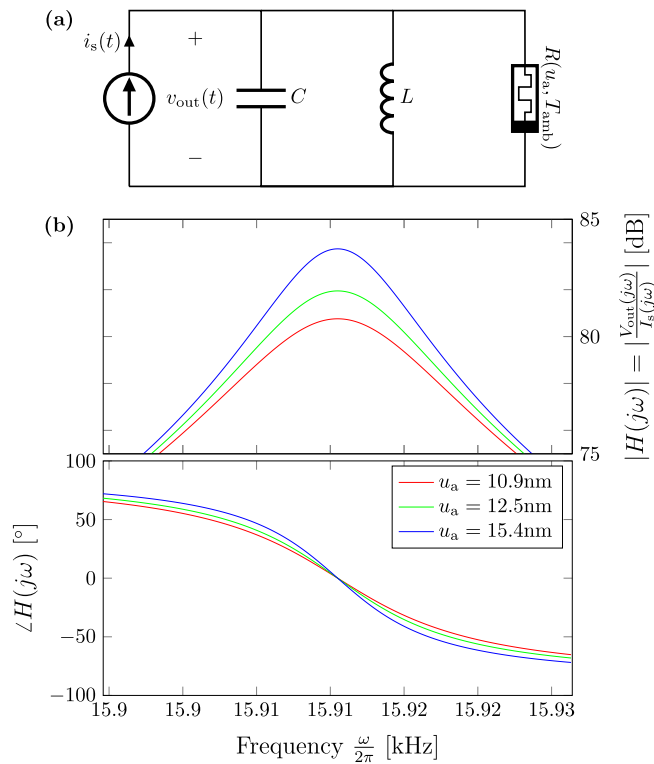


Figure 8. (a) Application in re-configurable electronics. Passive tunable RLC passband filter exploiting a PCM device in its read region via $R_m(u_a, T_{\text{int}})$. (b) Bode plots of the transfer function $H(j\omega)$ parametrized on the final resistance values reached by following the DRMs in Fig. 6.

coming from a sensor) and to be measuring the voltage drop $v_{\text{out}}(t)$ on the parallel RLC. For fixed values of the inductance L and capacitance C , the quality factor $Q = R_m(u_a, T_{\text{int}}) \sqrt{\frac{C}{L}}$ can be tuned to a desired value following the corresponding DRM in Fig. 6. Considering the Laplace-transformed port variables $I_s(j\omega) = \mathcal{L}(i_s(t))$ and $V_{\text{out}}(j\omega) = \mathcal{L}(v_{\text{out}}(t))$, Bode plots of the transfer function $H(j\omega) = \frac{V_{\text{out}}(j\omega)}{I_s(j\omega)}$ are reported in Fig. 8b parametrized on the final values reached by following the DRMs in Fig. 6. With C and L being fixed in the example to $1 \mu\text{F}$ and 0.1 mH respectively, it is evident how the quality factor, Q , can be modulated by first resetting the PCM cell and then setting it back with a constant SET current I . Similar applications can also be found in areas such as neuromorphic computing where the goal would be to tune synaptic weights in a neural network²⁹.

Conclusion

Phase-change memory is a highly promising post-CMOS technology that is finding applications as non-volatile memory, compute elements for in-memory and neuromorphic computing and also as components of reconfigurable electronic circuits. In this paper, we have developed a memristive state-dependent Ohm's law to describe the dynamics of PCM devices when SET write pulses are applied. This was based on the observation that the PCM dynamics is an intricate interconnection of electrical, thermal and structural dynamics. We developed a simulation model based on published literature as well as newly obtained experimental measurements on a mushroom-type PCM device. We also computed the dynamic route maps for the device upon the application of SET write pulses after initializing the devices to a certain RESET state. Finally, we experimentally measured the DRM with carefully executed experiments involving the successive application of short write pulses interspersed with read pulses. Given, the ultra-small timescales associated with the crystallization kinetics, this is a remarkable experimental feat and has helped establish an accurate memristive model to describe PCM dynamics. One of the crucial information drawn from the DRMs for PCM is the directed design of SET pulses to drive the thickness of the amorphous region and the associated low-field resistance. By exploiting the knowledge gained on the temporal evolution of the amorphous thickness, suitable SET pulses can be chosen to modulate dissipation in analog electronic circuits. As a case study we presented a PCM-based analog filter. This work is a significant step towards the inclusion of memristor-based PCM model in automatic design tools for programmable analog circuits and also for tunable synaptic elements in neuromorphic circuitry, overcoming the limitations posed by the complex dynamics of these elements.

Methods

Phase-change memory devices. The mushroom-type PCM devices used in the experiments were fabricated in the 90 nm CMOS technology node with the bottom electrode created via sublithographic key-hole process. The phase change material is doped $\text{Ge}_2\text{Sb}_2\text{Te}_5$. The dopant is primarily intended to enhance the endurance

of the PCM cell. The bottom electrode (BE) has a radius of ≈ 20 nm and length of ≈ 65 nm. The phase change material is ≈ 100 nm thick and extends to the top electrode (TE), the radius of which is ≈ 100 nm. In the same chip with the PCM devices, there is an integrated series resistor per device denoted by R_s which has a value of approx. 5.7 k Ω .

Experimental setup. For measurements that involve the application of fast pulses, an arbitrary waveform generator (AWG) was employed to apply the desired input stimulus and a Digital Storage Oscilloscope (DSO) to measure the current I and the applied voltage V_{applied} . The DSO acquired all the signals at a sampling frequency $f_s = 2.5$ GHz. An Agilent 81150A Pulse Function Arbitrary Generator was used and a Tektronix TDS3054B oscilloscope for AC voltage and current measurements. For slower steady-state $I - V$ measurements, a Keithley 2400 SMU was used. V_{applied} is directly measured by the DSO from the AWG. The resulting current that flows through the device is measured using a simple current to voltage conversion circuitry. Given the length of the wires (≈ 60 cm) and the involved time scales, the phase shift of current with respect to the V_{applied} signal has to be taken into account. The delay was estimated to be ≈ 6.4 ns.

Experimental measurement of DRM. Before performing each of the three measurements, the cell was reset with a $950 \mu\text{A}$ amplitude square pulse of $1 \mu\text{s}$ duration and sharp leading and trailing edges of 7.5 ns each. The reset was intended to create an amorphous dome of effective thickness, $u_a \approx 40$ nm. This initial u_a was estimated by fitting the $I - V_{\text{cell}}$ characteristics to a transport model proposed by Ielmini and Zhang³⁰. A train of interleaved write and read pulses were applied $20 \mu\text{s}$ after applying the reset pulse. Each write pulse with 7.5 ns leading and trailing edges had an amplitude of ≈ 2.93 V and a variable duration ranging between 25 ns and 121 ns). Each write pulse was followed, after 25 ns, by a read ramp voltage pulse of 0.5 V peak value and 50 ns duration. The reading voltage ramps had a 7.5 ns trailing edge and were followed by a new writing pulse after 25 ns.

Received: 24 November 2021; Accepted: 28 March 2022

Published online: 20 April 2022

References

- Kau, D. *et al.* A stackable cross point phase change memory. In *IEEE International Electron Devices Meeting (IEDM)*, 1–4 (IEEE, 2009).
- Disegni, F. *et al.* 16MB high density embedded PCM macrocell for automotive-grade microcontroller in 28 nm FD-SOI, featuring extension to 24MB for over-the-air software update. In *Symposium on VLSI Circuits*, 1–2 (IEEE, 2021).
- Wen, C.-Y. *et al.* A phase-change via-reconfigurable CMOS LC VCO. *IEEE Trans. Elect. Dev.* **60**, 3979–3988 (2013).
- Tuma, T., Le Gallo, M., Sebastian, A. & Eleftheriou, E. Detecting correlations using phase-change neurons and synapses. *IEEE Elect. Dev. Lett.* **37**, 1238–1241 (2016).
- Sebastian, A. *et al.* Tutorial: Brain-inspired computing using phase-change memory devices. *J. Appl. Phys.* **124**, 111101 (2018).
- Sebastian, A., Le Gallo, M. & Eleftheriou, E. Computational phase-change memory: beyond von Neumann computing. *J. Phys. D Appl. Phys.* **52**, 443002 (2019).
- Khaddam-Aljameh, R. *et al.* HERMES-core—a 1.59-TOPS/mm² PCM on 14-nm CMOS in-memory compute core using 300-ps/LSB linearized CCO-based ADCs. *IEEE J. Solid State Circuits* (2022).
- Khwa, W.-S. *et al.* A 40nm 2M-cell 8b-precision hybrid SLC-MLC PCM computing-in-memory macro with 20.5–65.0 TOPS/W for tiny AI edge devices. In: *International Solid-State Circuits Conference (ISSCC)* (IEEE, 2022).
- Burr, G. W. *et al.* Recent progress in phase-change memory technology. *IEEE J. Emerg. Select. Top. Circuits Syst.* **6**, 146–162 (2016).
- Le Gallo, M. & Sebastian, A. An overview of phase-change memory device physics. *J. Phys. D Appl. Phys.* **53**, 213002. <https://doi.org/10.1088/1361-6463/ab7794> (2020).
- Le Gallo, M., Athmanathan, A., Krebs, D. & Sebastian, A. Evidence for thermally assisted threshold switching behavior in nanoscale phase-change memory cells. *J. Appl. Phys.* **119**, 025704. <https://doi.org/10.1063/1.4938532> (2016).
- Chua, L. O. & Sung, M. K. Memristive devices and systems. *Proc. IEEE* **64**, 209–223. <https://doi.org/10.1109/PROC.1976.10092> (1976).
- Chua, L. Five non-volatile memristor enigmas solved. *Appl. Phys. A* **124**, 563. <https://doi.org/10.1007/s00339-018-1971-0> (2018).
- Ascoli, A., Messaris, I., Tetzlaff, R. & Chua, L. O. Theoretical foundations of memristor cellular nonlinear networks: stability analysis with dynamic memristors. *IEEE Trans. Circuits Syst. I Regul. Pap.* **67**, 1389–1401 (2019).
- Ascoli, A., Tetzlaff, R., Kang, S.-M. & Chua, L. O. Theoretical foundations of memristor cellular nonlinear networks: a drmm 2-based method to design memcomputers with dynamic memristors. *IEEE Trans. Circuits Syst. I Regul. Pap.* **67**, 2753–2766 (2020).
- Maldonado, D. *et al.* Experimental evaluation of the dynamic route map in the reset transition of memristive ReRAMs. *Chaos Solitons Fractals* **139**, 110288 (2020).
- Nardone, M., Simon, M., Karpov, I. V. & Karpov, V. G. Electrical conduction in chalcogenide glasses of phase change memory. *J. Appl. Phys.* **112**, 071101. <https://doi.org/10.1063/1.4738746> (2012).
- Kroezen, H. J. *et al.* Schottky barrier formation at amorphous-crystalline interfaces of GeSb phase change materials. *Appl. Phys. Lett.* **100**, 094106. <https://doi.org/10.1063/1.3691179> (2012).
- Sebastian, A., Le Gallo, M. & Krebs, D. Crystal growth within a phase change memory cell. *Nat. Commun.* **5**, 4314. <https://doi.org/10.1038/ncomms5314> (2014).
- Secco, J., Corinto, F. & Sebastian, A. Flux-charge memristor model for phase change memory. *IEEE Trans. Circuits Syst. II Exp. Briefs* **65**, 111–114. <https://doi.org/10.1109/TCSII.2017.2701282> (2018).
- Le Gallo, M., Krebs, D., Zipoli, F., Salinga, M. & Sebastian, A. Collective structural relaxation in phase-change memory devices. *Adv. Elect. Mater.* **4**, 1700627 (2018).
- Ongaro, R. & Pillonnet, A. Synthetic theory of poole and poole-frenkel (pf) effects. *IEE Proc. A (Sci. Measur. Technol.)* **138**, 127–137(10). <https://doi.org/10.1049/ip-a-3.1991.0018> (1991).
- Frenkel, J. On pre-breakdown phenomena in insulators and electronic semi-conductors. *Phys. Rev.* **54**, 647–648 (1938).
- Shih, Y. H. *et al.* Understanding amorphous states of phase-change memory using frenkel-poole model. In *Proceedings of the 2009 IEEE International Electron Devices Meeting (IEDM)*, 1–4. <https://doi.org/10.1109/IEDM.2009.5424229> (2009).
- Hill, R. M. Poole-frenkel conduction in amorphous solids. *Philos. Mag. J. Theor. Exp. Appl. Phys.* **23**, 59–86. <https://doi.org/10.1080/14786437108216365> (1971).
- Hartke, J. L. The three-dimensional poole-frenkel effect. *J. Appl. Phys.* **39**, 4871–4873. <https://doi.org/10.1063/1.1655871> (1968).

27. Betti Beneventi, G., Guarino, L., Ferro, M. & Fantini, P. Three-dimensional poole-frenkel analytical model for carrier transport in amorphous chalcogenides. *J. Appl. Phys.* **113**, 044506. <https://doi.org/10.1063/1.4788798> (2013).
28. Le Gallo, M., Kaes, M., Sebastian, A. & Krebs, D. Subthreshold electrical transport in amorphous phase-change materials. *New J. Phys.* **17**, 093035 (2015).
29. Sebastian, A., Le Gallo, M., Khaddam-Aljameh, R. & Eleftheriou, E. Memory devices and applications for in-memory computing. *Nat. Nanotechnol.* **15**, 529–544 (2020).
30. Ielmini, D. & Zhang, Y. Analytical model for subthreshold conduction and threshold switching in chalcogenide-based memory devices. *J. Appl. Phys.* **102**, 054517. <https://doi.org/10.1063/1.2773688> (2007).

Acknowledgements

AS and BK acknowledge funding from the European Research Council (ERC) under the European Union's Horizon 2020 research and innovation programme (grant agreement number 682675). FC acknowledges the support by the Ministero dell'Istruzione, dell'Università e della Ricerca (MIUR) under contract 2017LSCR4K-003. LC is supported by USA grant No. FA 9550-18-0016. This article/publication is based upon work from COST Action IC1401, supported by COST (European Cooperation in Science and Technology). Weblink: www.cost.eu

Author contributions

F.C., A.S. and L.C. defined the research direction and supervised the project. F.M. performed the experiments with assistance from B.K. and M.L.G. and together with J.S. developed the mathematical models. F.M., J.S., F.C. and A.S. wrote the manuscript with input from all authors.

Competing interests

The authors declare no competing interests.

Additional information

Correspondence and requests for materials should be addressed to F.M., F.C. or A.S.

Reprints and permissions information is available at www.nature.com/reprints.

Publisher's note Springer Nature remains neutral with regard to jurisdictional claims in published maps and institutional affiliations.



Open Access This article is licensed under a Creative Commons Attribution 4.0 International License, which permits use, sharing, adaptation, distribution and reproduction in any medium or format, as long as you give appropriate credit to the original author(s) and the source, provide a link to the Creative Commons licence, and indicate if changes were made. The images or other third party material in this article are included in the article's Creative Commons licence, unless indicated otherwise in a credit line to the material. If material is not included in the article's Creative Commons licence and your intended use is not permitted by statutory regulation or exceeds the permitted use, you will need to obtain permission directly from the copyright holder. To view a copy of this licence, visit <http://creativecommons.org/licenses/by/4.0/>.

© The Author(s) 2022